

Contextual responses drive a unique laminar signature in human V1

Jurjen Heij^{1,2,3*}, Luisa Raimondo^{1,2,3}, Jeroen C.W. Siero^{1,2,4}, Wietske van der Zwaag^{1,2}, Tomas Knapen^{1,2,3}, and Serge O. Dumoulin^{1,2,3,5}

¹Spinoza Centre for Neuroimaging, Amsterdam, Netherlands

²Department of Computational Cognitive Neuroscience and Neuroimaging, Netherlands Institute for Neuroscience, Royal Netherlands Academy for Arts and Sciences, Amsterdam, Netherlands

³Department of Experimental and Applied Psychology, Vrije Universiteit Amsterdam, Amsterdam, Netherlands

⁴Department of Radiology, University Medical Center Utrecht, Utrecht, Netherlands

⁵Department of Experimental Psychology, Utrecht University, Amsterdam, Netherlands

*Correspondence: j.heij@herseninstituut.knaw.nl

SUMMARY

Neuronal populations in visual cortex balance stimulus-driven retinal input and context-related input from neighboring neurons. These two types of input are transmitted by cortical connections terminating in different layers of the cortex. Thus, cortical layers provide a unique window into the balance of stimulus-driven versus context-related computations. Here, we combined novel line-scanning fMRI with a new cortical targeting approach to record responses across cortical depth in unprecedented detail in living humans. We recorded signals from a specific patch of cortex of each individual participant and custom-designed stimuli to the population receptive field (pRF) properties of this cortical patch. Biasing the balance toward the stimulus-driven input elicited strong responses across the entire cortical depth with response amplitudes increased toward the pial surface. In contrast, stimulation with contextual stimuli elicited responses at superficial and deeper cortical depths in alignment with termination sites of descending connections predicted from anatomical and electrophysiological experiments. These findings draw direct links between invasive animal neurophysiological studies and human neuroimaging. The non-invasive nature of our experimental setup opens the door to measurements of cognitive manipulation in humans.

KEYWORDS

line-scanning, pRF, laminar, ultra-high field MRI, 7T, BOLD fMRI, context, divisive normalization

INTRODUCTION

31

Neurons in early visual cortex respond to a particular part of the visual field, i.e., the population receptive field^{1–3}. The responses of these neurons do not rely on stimulus-driven input only but is complemented by integrating context-related responses from neighboring neurons^{4–7} (Figure 1, top panels). In divisive normalization (DN) computational models, the response of these neurons is modeled by the ratio of two components (Figure 1, middle panels): stimulus drive (or activation component) and contextual integration (or normalization component)^{7–9}. These DN models capture a variety of contextual responses, including for example surround suppression and response compression^{7–13}. From a biological perspective, the DN models cannot be explained by ascending connections alone, i.e., such computations require descending connections between neurons and neighboring areas^{5,6,14–16}.

Ascending and descending connections terminate in specific layers of the cortex (Figure 1, bottom panels)^{17,18}. Indeed, invasive macaque neurophysiology studies showed that stimuli inside the classical pRF elicited the earliest response in layer 4 of primary visual cortex (V1)^{5,14,19–22}. These responses are driven by ascending connections originating from the lateral geniculate nucleus (LGN)^{23,24}. Responses to stimuli outside the classical pRF are mediated by descending connections from neighboring neurons/areas to superficial and deeper layers of V1^{5,6}. The further away stimulation from the classical pRF, the more responses originate from superficial and deeper layers¹⁹. This layer-specific response pattern is thought to reflect contributions to lateral (near-surround) and descending (far-surround) connections^{4,12,25}. Thus, responses to stimuli biasing the activation/normalization balance should therefore drive different laminar connections (Figure 1, middle panels).

41

42

43

44

45

46

47

48

49

50

51

52

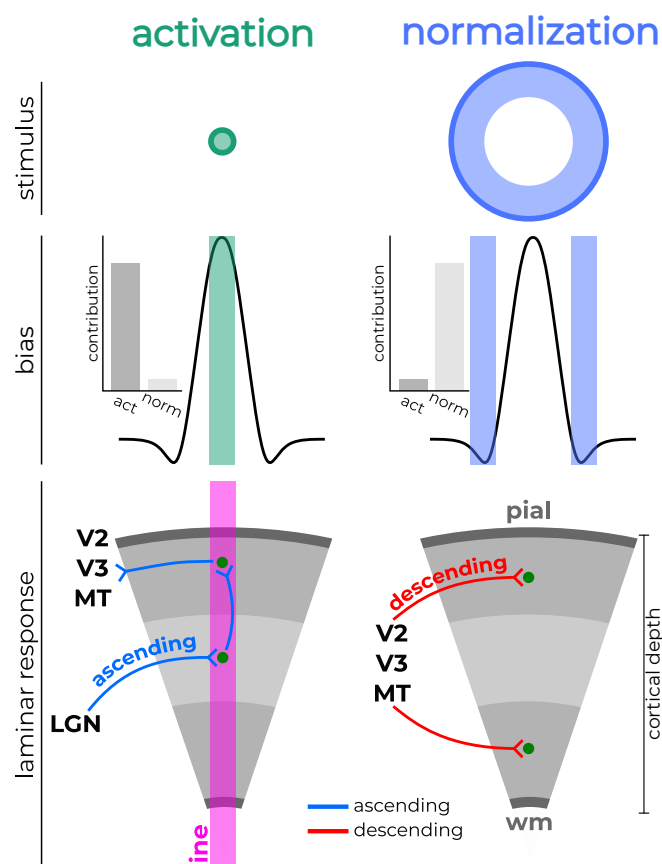


Figure 1: Laminar connectivity in V1. Stimuli falling in the classical population receptive field (pRF) are biased toward the *activation* pool. These signals are transmitted via ascending connections from the lateral geniculate nucleus (LGN) that terminate predominantly in the middle layer (blue). These signals are then propagated through intralaminar fibers toward the surface and to neighboring regions. Stimuli on the flanks of the classical pRF are biased toward the *normalization* pool that send contextual information from neighboring areas back to superficial and deep layers via descending connections (red). Thus, cortical layers provide a unique window into the balance of stimulus-driven versus context-related computations. With line-scanning fMRI (purple rectangle), we can record responses across cortical depth to custom-designed stimuli biasing the activation/normalization balance in humans with unprecedented detail.

High-resolution functional MRI (fMRI) permits access to the different layers of the cortex^{26,27}. This cortical depth-resolved fMRI enables researchers to study the flow of information through

53

54

the cortex^{28,29}. Contemporary fMRI acquisitions typically sample the cortex with ± 0.8 millimeter isotropic resolutions^{26,27,30–33}. At this resolution, the entire cortical depth is covered by about 2–3 data points (voxels), resulting in substantial signal mixing from multiple layers^{34,35}. To improve spatial precision across cortical depth, we need acquisitions with higher resolutions. Line-scanning fMRI sacrifices spatial coverage for resolution in order to sample responses from a specific patch of cortex with ultra-high spatial resolution (250 μm along cortical depth)^{36–38}. The high spatial resolution means the cortical depth of a specific patch is covered by 6–10 data points. Akin to animal neurophysiology, we can then design our experiments to target the functional properties of this cortical patch^{14,19}. Using our established selection targeting method³⁹, we generated stimuli specifically tailored to the functional properties derived from computational modeling of the participants' targeted patch of cortex in visual cortex. These stimuli were differentially biased toward the activation/normalization balance. Combining ultra-high spatial resolution and our functional targeting approach brings us in a unique position to measure cortical depth-resolved responses and bridge human fMRI with non-human primate electrophysiology.

RESULTS

Cortical-patch specific stimuli evoke differential responses

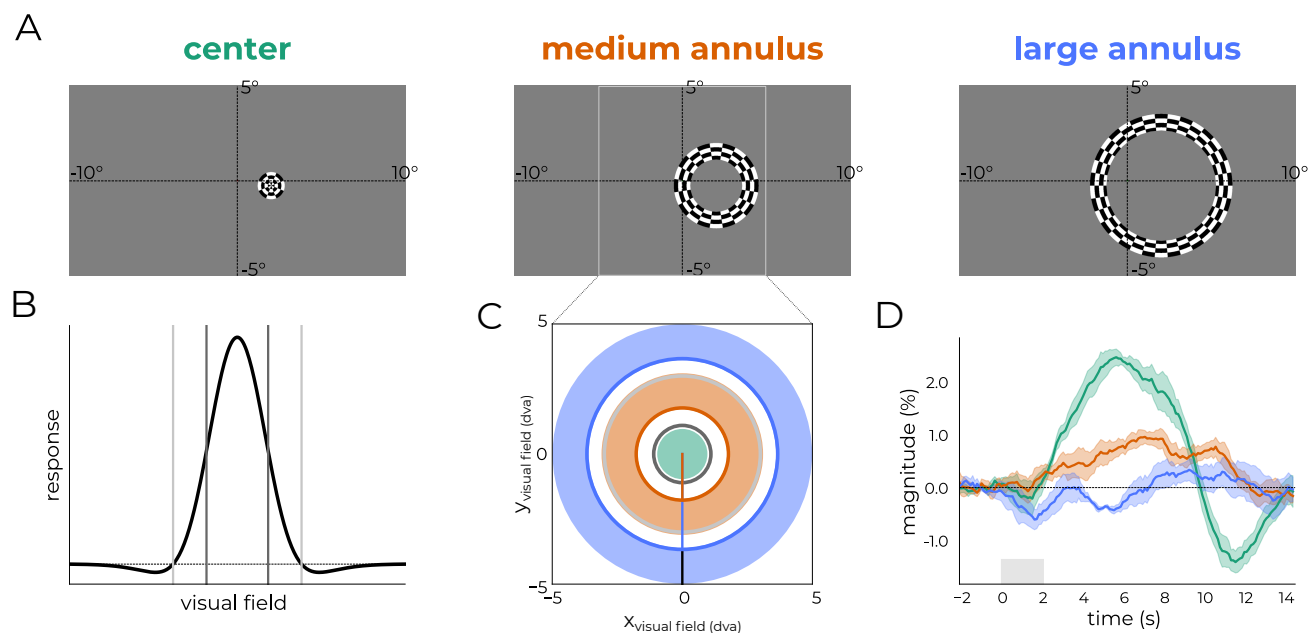


Figure 2: Participant-specific stimulus design procedure. (A) Example stimuli as presented on the screen, targeting the location in visual space that is encoded by the target cortex patch. (B) Spatial response profile of target pRF with full-width at half-maximum (FWHM) denoted with dark gray bands and zero-crossings in light gray. (C) From the location of the target pRF (x , y) in visual space, we determined the smallest distance to the edge of the screen ($x_{\text{visual field}}$ or $y_{\text{visual field}}$) behind the MRI bore in order to present the largest stimulus possible without occlusion. The radius for the large stimulus (blue) was set to this distance (orange line + blue line + black line). The radius for the medium stimulus (orange) was set to be halfway of the distance between the center stimulus and large annulus. (D) Response profiles for the different stimuli averaged across the cortical depth for a representative participant (see Figure S2 for all participants).

Each participant was presented with a unique set of stimuli designed on the functional organization of the target patch (see Figure 2A, Figure S1). We deduced where the zero-crossing and full-width half-max were located for each target pRF to highlight the stimulus configurations relative to the properties of the target pRF (Figure 2B). We then derived the size-tuning curves through simulations by passing stimuli of increasing sizes ranging from 0 to 10 degree-of-visual angle (dva) to the estimates of the pRFs^{7,11,40–42}. Based on the size-tuning curve, we derived three stimuli that were all centered on the pRF (Figure 2C), but differentially biased the activation/normalization balance (Figure 1, middle panels), resulting in distinct responses (Figure 2D):

1) *center* stimulus (green). This stimulus consisted of a radial checkerboard stimulus with the size that elicited the maximum response according to the size-tuning curve (i.e., maximally biased toward the activation pool); 2) *large annulus* (blue). This stimulus consisted of a concentric ring subtending 2 dva stimulating as much of the normalization pool of the pRF as permitted by the physical dimensions of the screen. From the location of the target pRF in visual space, we drew the largest possible, non-occluded stimulus. The shortest distance served as the radius of the stimulus; 3) *medium annulus* (orange). Similar to stimulus II, this stimulus consisted of a 2 dva wide concentric ring with a radius halfway of the distance between the center and large annulus stimulus, preferably without spatial overlap with the other stimuli. All stimuli had 2 radial cycles per degree stimulus size, and 1 angular cycle per degree stimulus size. In case parts of the screen were obstructed by the MR setup (e.g., transmit boxes, eye-tracker, MRI bore), we iteratively adjusted the stimuli based on verbal feedback from participants to ensure the stimuli were not occluded (Figure 2C).

To verify the responses localized to the intended target locations, we first averaged all the responses from data points across cortical depth and runs with identical timing (see Methods details: Experimental setup). Response profiles were extracted from a time window starting 2 seconds prior to stimulus onset to 14 seconds after. This resulted in 2 (effective runs with different event timings) x 5 (events per run) profiles for each stimulus for each participant. The stimulus eliciting the largest response in the target pRF according to the computational model indeed resulted in the largest response of all stimuli (Figure S2). To formally test the response magnitude across events, we averaged the response over a time period around the peak of the response to the *center* stimulus (Figure S2, insets) and entered this into a linear mixed-effects model (Table S1). The model demonstrated significant different between stimulus types ($p < 0.001$). Using Tukey HSD pairwise comparisons, we found that the estimated mean response for the center stimulus (1.48 ± 0.094) was significantly higher than the response to the medium annulus (-1.22 ± 0.087) ($\Delta = 1.22$, $95\%CI = 1.00-1.44$, $p < 0.001$) and large annulus (-1.36 ± 0.087) ($\Delta = 1.36$, $95\%CI = 1.14-1.58$, $p < 0.001$). The difference in mean response between the medium and large annulus was not significant ($\Delta = -0.14$, $95\%CI = -0.36-0.07$, $p = 0.27$). This confirms that the line was positioned in the cortical patch with the selected pRF.

Context drives responses at superficial and deeper depths

The number of data points across cortical depth of the target patch varied across participants due to differences in cortical thickness (6-10 data points). We therefore regridded the data so that 20 data points covered the cortical depth in all participants (note that the spatial autocorrelation is still less compared to interpolating 2–3 data points to 20 depths^{30,34,35,43–45}). We then produced depth-by-time plots colored by magnitude to show the response evolution across time and depth (Figure 3, left and middle column)³⁶. The center stimulus (biased toward the activation pool) elicited a clear positive BOLD response across all cortical depths. In contrast, the response to the large annulus (biased toward the normalization pool) was markedly different (Figure 3;

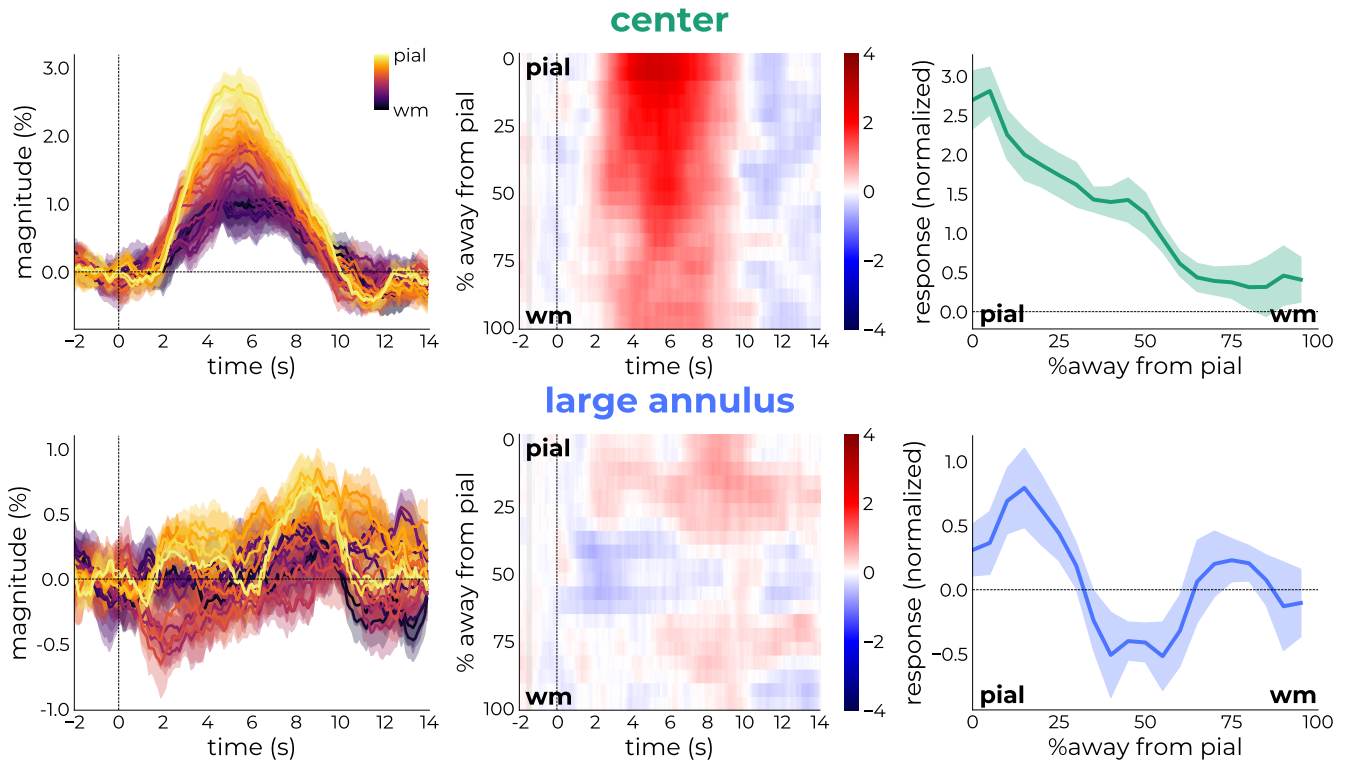


Figure 3: For the center (green) and large annulus (blue), the response evolution as time courses (left column) and depth-by-time (middle column). The right column represents the projection of the average profile to the center stimulus (biased toward the activation pool), showing responses across all cortical depths with stronger response toward the surface (pial). The large annulus (biased toward the normalization pool) elicited positive responses more reserved to superficial and deeper depths with negative responses at middle (input) depths. These results are in line with electrophysiological and anatomical predictions about the laminar distribution of contextual integration. Shaded error represents 95% confidence intervals ($\pm \text{SEM} \times 1.96$).

bottom row). We observed a negative deflection at middle depths, flanked by positive peaks at superficial and deeper depths (Figure 3; bottom row, middle column). To visualize this effect more clearly, we projected the responses to the center stimulus averaged across cortical depth to the response profiles of the other stimuli. In other words, we aimed to find a scaling between the cortical depth-dependent profiles and the participants' average profile to the center stimulus across cortical depth (Figure S3, green profile in bottom right panel, *average*). This effectively collapsed the depth-by-time plots over the time dimension. A high value is assigned if the average profile is strongly represented in the profile of individual depths, a low value if the opposite is true. To remove noise, we normalized the profiles by subtracting the participant's individual mean from the profiles and adding back the mean across participants. For the response to the center stimulus, responses toward the superficial surface (pial) were more strongly represented by the average profile compared to deeper depths (wm), a pattern often observed in the laminar fMRI literature^{29,39,46–51}. The response profile to the large annulus, on the other hand, showed a relatively strong initial peak at superficial depths, followed by a deflection at middle depths and another putative peak at deeper depths (see Figure S3A for participant-specific profiles for the right column). This was not an artifact of the voxel selection (Figure S3B, Figure S10), normalization strategy (Figure S3C), or interpolation (Figure S4). These results point to distinct laminar responses to stimulus biased toward activation (center) or normalization (large annulus).

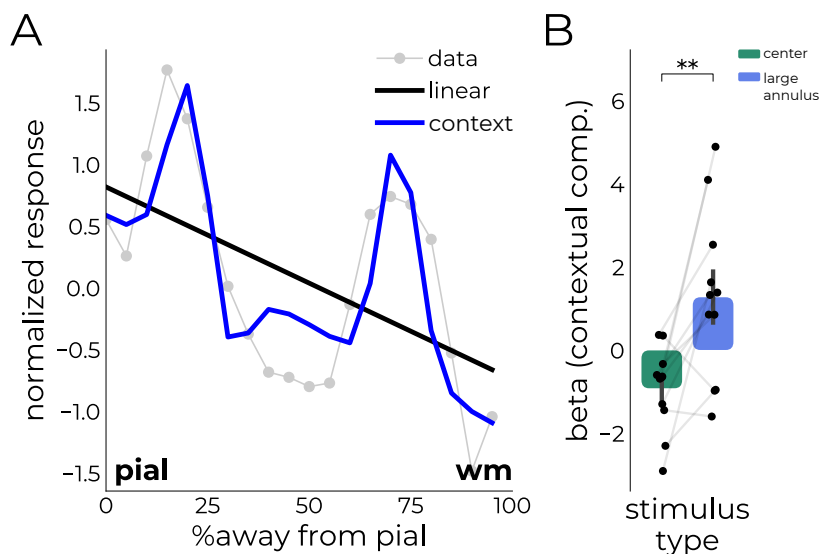


Figure 4: Modeling contextual integration across cortical depth for the large annulus. (A) Laminar profile of the large annulus (gray) and model fits from the *linear* (black) and *contextual* (blue) model components, representing the laminar distribution of normalization processing. (B) Comparison of summed beta-estimates from the contextual model components for center and large annulus stimuli. $**p < .01$.

To quantify this effect, we defined a model that included a linear component (as evoked by the center stimulus) and two Gaussian distributions representing the peaks at superficial and deep cortical depths (Figure 4A). This model was based on 1) the observation the descending connections carrying context-related information from higher order areas is received in superficial and deeper layers of V1^{17,52} and 2) findings from an earlier animal electrophysiological experiment that used a strikingly similar setup and found activation in these layers in response to a large annulus¹⁹. Derivative components were added to each Gaussian distribution to account for individual differences in anatomy of the target patch. This allowed the peaks to slightly move. We then summed the beta-values from the context-related model components (double peak and derivatives, excluding the linear term) which allowed us to quantify the extent to which a response was driven by the activation (stimulus-drive) or normalization (contextual integration) pool (Figure 4B, Figure S5). A one-way ANOVA revealed a significant main effect of stimulus type ($F_{1,20}=15.34$, $p < 0.001$, partial $\eta^2=0.43$), wherein the large annulus stimulus had higher t-stat values for the contextual component of the model (1.63 ± 0.61) compared to the center stimulus (-1.18 ± 0.38), $t_{10}=4.01$, $p=.002$, Cohen's $d=1.37$. This suggests that stimuli targeting predominantly the normalization pool elicited context-related responses at sites where descending feedback connections terminate, whereas stimuli targeting the activation pool elicited less depth-specific stimulus-driven responses.

Medium annulus response resembled large annulus response

In the previous section, we looked at responses to the extremes of the activation/normalization balance; stimuli were maximally biased to either the activation (center stimulus) or normalization pool (large annulus stimulus). Thus, presenting a stimulus that is somewhere in between should elicit a response pattern somewhere in between (medium annulus). Indeed, the response profile of the medium annulus mostly resembled the large annulus, with stronger responses away from middle depths (Figure 5). The response peak was not as far toward the surface (pial) compared to the large annulus response (Figure 4, bottom right panel). We subjected the laminar profiles to the medium annulus to the same model as described above (Figure 6A, Figure S6). A one-way ANOVA across including all stimulus types revealed a significant main effect of stimulus type on the beta values from the context-related model components ($F_{2,30}=7.11$, $p=0.003$, partial

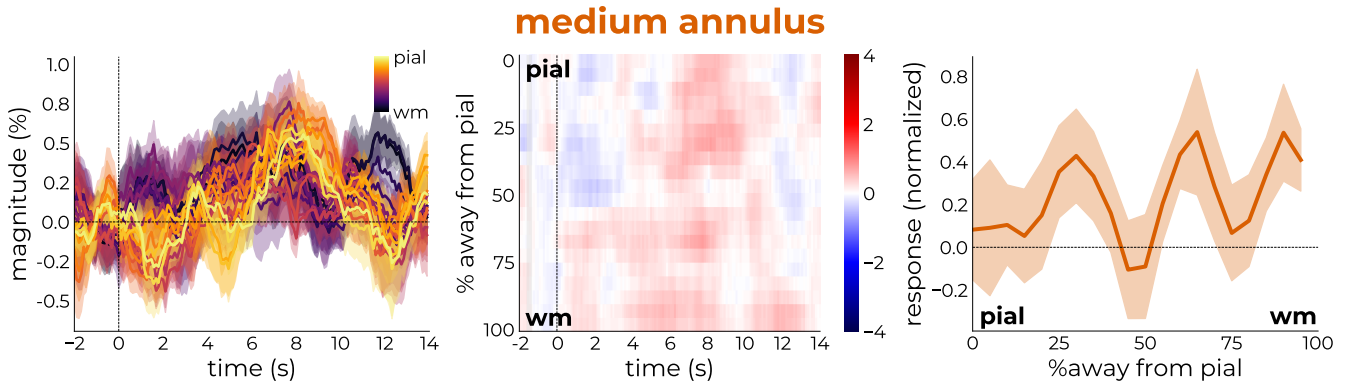


Figure 5: Response evolution as time courses (left column) and depth-by-time (middle column) for the medium annulus, a stimulus halfway between the center and large annulus. The right column represents the projection of the profile of the center stimulus averaged over cortical depth and participants (Figure 3, top right panel). Whereas the large annulus elicited response close to superficial depths ($\sim 15\%$ away from pial surface, Figure 3, bottom right panel), the medium annulus elicited responses in multiple sites across cortical depth. Shaded error represents 95% confidence intervals ($\pm \text{SEM} \times 1.96$).

$\eta^2=0.32$). Post-hoc analysis with Holm's correction revealed that the context-related component was higher for the medium annulus (0.75 ± 0.38) compared to the center stimulus (-1.18 ± 0.38), $t_{10}=3.15$, $p=.03$, Cohen's $d=1.51$. After correction, the difference between the large annulus and center stimulus remained significant ($t_{10}=4.01$, $p=.007$, Cohen's $d=1.37$). The effect between the large and medium annulus was not significant ($p=0.22$). These results highlight the similarity of the cortical signature evoked by stimuli that drive context-related inputs compared to stimuli that drive stimulus-driven inputs.

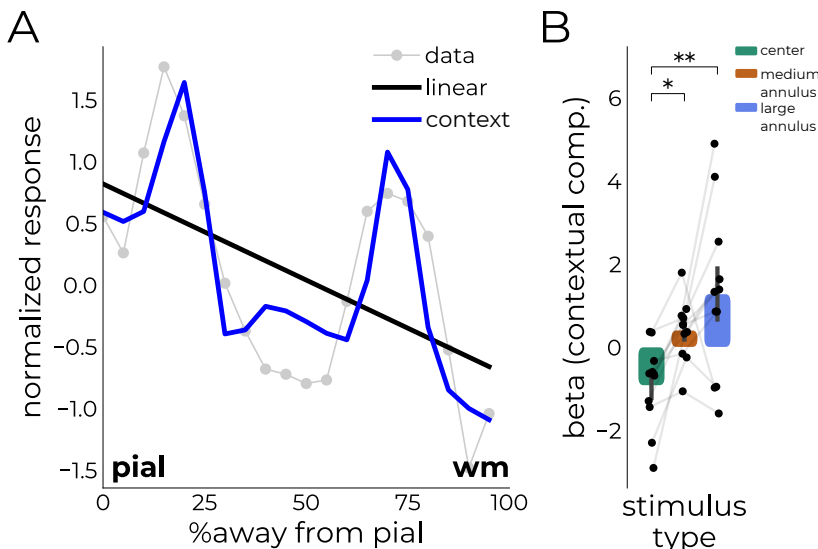


Figure 6: Modeling contextual integration across cortical depth for the medium annulus. (A) Laminar profile of the large annulus (gray) and model fits from the *linear* (black) and *contextual* (blue) model components. (B) Comparison of summed beta-estimates from the contextual model components for all events (center and large annulus taken from Figure 4B). $**p<0.01$, $*p<0.05$.

DISCUSSION

173

Probing contextual responses with line-scanning fMRI

174

Divisive Normalization (DN) is found across the brain in multiple systems^{8,9,53–56}. DN is therefore often thought of as a canonical computational operation that the brain uses for different purposes⁹. Central to DN is that the output of a given neuron not only depends on its direct stimulation (activation) component, but also on the integration of signals from nearby neurons (normalization component). These processes inform us about the nature of feedforward and feedback processes; the activation component is driven by ascending bottom-up connections terminating in the middle layers of the cortex^{23,24,57,58}. Contextual integration from neighboring neurons/areas arises from descending feedback connections terminating in the superficial and deeper layers of the cortex^{5,6,17,18}. Thus, biasing the activation/normalization balance could reveal processing circuits within the layers of the cortex. In this study, we applied our selection and targeting framework to probe such responses in humans using ultra-high resolution line-scanning fMRI³⁹. This was done by targeting a patch of cortex with specific functional properties and present stimuli designed using computational modeling that were differentially biased toward the activation or normalization component. We show that cortical depth-dependent responses differed depending on the bias toward activation or normalization.

175
176
177
178
179
180
181
182
183
184
185
186
187
188
189

Distinct context-dependent laminar signature

190

Stimuli designed maximally biased toward the activation pool (*center*) elicited responses across the cortical depth, whereas responses to stimuli biased toward the normalization pool (*large annulus*) were preferentially localized in the superficial and deeper cortical depths (Figure 3). Many studies have attempted to separate feedforward from feedback processing, but direct comparison is rendered complicated due to different experimental paradigms. Such paradigms include texture-segmentations¹⁴, low-spatial frequency stimuli²¹, high-contrast drifting gratings⁵⁹, and line segments²². Differences in experimental setup will target different neuronal populations across cortical depth, often resulting in differences in the laminar profile of spiking⁶⁰. Yet, Bijanzadeh and colleagues¹⁹ performed a study with many similarities to the experimental setup presented in this work: In an attempt to study surround suppression, a special category of divisive normalization, they simultaneously recorded responses across cortical depth to a similar set of stimuli: a stimulus inside the classical RF, an annulus stimulating the near surround, and an annulus stimulating the far surround. The similarities in experimental setups (targeting of a specific (p)RF, designing stimuli biasing the activation/normalization balance, and measuring responses simultaneously across depth) allows for a clear comparison between non-human primate electrophysiology¹⁹ and human fMRI (current work). Similarly, they found that responses to stimuli biased toward normalization were constraint to superficial and deeper layers of the cortex; layers where descending connections carrying context-related information from neighboring regions terminate^{17,18}. In contrast, they also observed the earliest activation in the middle layers in response to the activation stimulus. In the current study, we observed activation across all cortical depths. The speed with which these signals are transmitted makes it complicated to capture using BOLD fMRI^{14,21,60}. Faster acquisitions may be able to capture such responses^{27,36,61,62}. Nevertheless, the distinct signature of context-related processing across cortical depth may still prove useful in disentangling ascending from descending connections. The similarities in experimental design and outcome moreover highlight the possibility to link animal electrophysiological experiments with non-invasive human fMRI experiments.

191
192
193
194
195
196
197
198
199
200
201
202
203
204
205
206
207
208
209
210
211
212
213
214
215
216

Limitations of this study

The effective resolution of line-scanning is impacted by the amount of curvature of the targeted cortical sheet^{63–65}, participant motion^{66,67}, quality of saturation slabs³⁷, targeting success³⁹, and positioning relative to the surface coils used for MR signal detection^{68,69}. This particular setup is further complicated by the presentation of circular, flickering checkerboard stimuli designed based on pRFs that are estimated using a bar-sweep configuration^{2,26}, a different sequence²⁶, on different days^{70–73}, and with different levels of thermal noise^{74–76}; all factors affecting the neuronal population (and therefore pRF) is eventually targeted^{26,71,77}. The pRF stimulus with bar-configurations is predominantly a spatial design that ignores the time dimension. With the current setup, stimuli stimulate the activation/normalization pool for a much shorter period (2 seconds) compared to the bar-configuration (15–20 seconds). It is not entirely clear how such changes in temporal characteristics of stimuli affect the processing dynamics across cortical depth. Lastly, the vast reduction of the field-of-view during line-scanning imposes restrictions on its utility on a larger scale (i.e., between-area communication).

Bridging neurophysiology and fMRI

In this work, we applied the selecting and targeting framework of line-scanning to study divisive normalization across cortical depth. This strategy mimics invasive electrophysiological setups where a known target is probed across depth with electrodes. Using existing pRF data, we tailored stimuli for each participant uniquely to maximally probe the activation and normalization pools. The advantage of such an approach is that (i) cortical depth is sampled by many more data points (6-10 vs. 2-3), thereby reducing partial voluming and effects from large veins and; (ii) a specific patch of cortex could be targeted, improving the specificity of the experimental paradigm. We show that the stimulus biased toward the activation pool (center stimulus) elicited the strongest response of all stimuli across all depths, with stronger responses toward the cortical surface. In contrast, stimuli biased toward the normalization pool elicited responses much more constrained to superficial and deeper depths; sites where descending context-related connections from neighboring areas terminate. These results are corroborated by animal studies and computational work, showcasing the possibility to draw direct links between animal studies or methodologies and human work. The non-invasive nature of this experimental setup opens the door to probing cognitive manipulations in humans.

Supplemental information index 247

Figures S1-S8, Table S1, and their legends in a PDF 248

Acknowledgments 249

This work was supported by a Royal Netherlands Academy for Arts and Sciences (KNAW) grant (2018, to Serge O. Dumoulin, Wietske van der Zwaag, Jeroen C.W. Siero, Tomas Knapen), a Netherlands Organization for Scientific Research (NWO) Vidi Grant (TTW VI. Vidi.198.016 to Wietske van der Zwaag), an NWO Vici grant (016. Vici.185.050 to Serge O. Dumoulin). The Spinoza Centre is a joint initiative of the KNAW—Netherlands Institute for Neuroscience, Vrije University Amsterdam, Amsterdam University Medical Centra—locations AMC and VUmc. 250
251
252
253
254
255

Author contributions 256

Conceptualization, T.K. & S.O.D.; methodology, J.H., T.K. & S.O.D.; investigation, J.H.; writing – original draft, J.H.; writing – review & editing, J.H., L.R., J.C.W.S., W.Z., T.K., & S.O.D.; funding acquisition, J.C.W.S., W.Z., T.K., & S.O.D.; resources, W.Z., T.K., & S.O.D. 257
258
259

Declaration of interests 260

The authors declare no competing interests. 261

References

1. Victor, J. D., Purpura, K., Katz, E., and Mao, B. (1994). Population encoding of spatial frequency, orientation, and color in macaque V1. *J Neurophysiol* 72, 2151–2166. doi:10.1152/jn.1994.72.5.2151.
2. Dumoulin, S. O., and Wandell, B. A. (2008). Population receptive field estimates in human visual cortex. *NeuroImage* 39, 647–660. doi:10.1016/j.neuroimage.2007.09.034.
3. Brewer, A. A., Liu, J., Wade, A. R., and Wandell, B. A. (2005). Visual field maps and stimulus selectivity in human ventral occipital cortex. *Nat Neurosci* 8, 1102–1109. doi:10.1038/nn1507.
4. Angelucci, A., Levitt, J. B., Walton, E. J., Hupé, J. M., Bullier, J., and Lund, J. S. (2002). Circuits for local and global signal integration in primary visual cortex. *J Neurosci* 22, 8633–8646. doi:10.1523/jneurosci.22-19-08633.2002.
5. Angelucci, A., and Sainsbury, K. (2006). Contribution of feedforward thalamic afferents and corticogeniculate feedback to the spatial summation area of macaque V1 and LGN. *J Comp Neurol* 498, 330–351. doi:10.1002/cne.21060.
6. Nurminen, L., Merlin, S., Bijanzadeh, M., Federer, F., and Angelucci, A. (2018). Top-down feedback controls spatial summation and response amplitude in primate visual cortex. *Nat Commun* 9. doi:10.1038/S41467-018-04500-5.
7. Aqil, M., Knapen, T., and Dumoulin, S. O. (2021). Divisive normalization unifies disparate response signatures throughout the human visual hierarchy. *Proc. Natl. Acad. Sci. U.S.A.* 118. doi:10.1073/pnas.2108713118.
8. Heeger, D. J. (1992). Normalization of cell responses in cat striate cortex. *Vis Neurosci* 9, 181–197. doi:10.1017/S0952523800009640.
9. Carandini, M., and Heeger, D. J. (2012). Normalization as a canonical neural computation. *Nat Rev Neurosci* 13, 51–62. doi:10.1038/nrn3136.
10. Sullivan, T. J., and De Sa, V. R. (2006). A model of surround suppression through cortical feedback. *Neural Networks* 19, 564–572. doi:10.1016/j.neunet.2005.12.003.
11. Nassi, J. J., Lomber, S. G., and Born, R. T. (2013). Corticocortical Feedback Contributes to Surround Suppression in V1 of the Alert Primate. *J Neurosci* 33, 8504–8517. doi:10.1523/JNEUROSCI.5124-12.2013.
12. Angelucci, A., and Shushruth, S. (2013). Beyond the classical receptive field: surround modulation in primary visual cortex. *New Vis Neurosci* (425–444).
13. Blakemore, C., and Tobin, E. (1972). Lateral inhibition between orientation detectors in the cat's visual cortex. *Exp Brain Res* 15. doi:10.1007/BF00234129.
14. Self, M. W., van Kerkoerle, T., Supér, H., and Roelfsema, P. R. (2013). Distinct Roles of the Cortical Layers of Area V1 in Figure-Ground Segregation. *Curr Biol* 23, 2121–2129. doi:10.1016/j.cub.2013.09.013.
15. Lamme, V. A. F., and Roelfsema, P. R. (2000). The distinct modes of vision offered by feedforward and recurrent processing. *Trends Neurosci* 23, 571–579. doi:10.1016/S0166-2236(00)01657-X.

16. Lamme, V. A. (1995). The neurophysiology of figure-ground segregation in primary visual cortex. *J Neurosci* *15*, 1605–1615. doi:10.1523/JNEUROSCI.15-02-01605.1995. 302
303
17. Felleman, D. J., and Van Essen, D. C. (1991). Distributed hierarchical processing in the primate cerebral cortex. *Cereb Cortex* *1*, 1–47. doi:10.1093/cercor/1.1.1. 304
305
18. Hubel, D. H., and Wiesel, T. N. (1972). Laminar and columnar distribution of geniculocortical fibers in the macaque monkey. *J Comp Neurol* *146*, 421–450. doi:10.1002/cne.901460402. 306
307
308
19. Bijanzadeh, M., Nurminen, L., Merlin, S., Clark, A. M., and Angelucci, A. (2018). Distinct Laminar Processing of Local and Global Context in Primate Primary Visual Cortex. *Neuron* *100*, 259–274.e4. doi:10.1016/j.neuron.2018.08.020. 309
310
311
20. Blasdel, G., and Lund, S. (1983). Termination of Afferent Axons in Macaque Striate Cortex. *J Neurosci* *3*. doi:10.1073/pnas.2108713118. 312
313
21. Schroeder, C. E., Mehta, A. D., and Givre, S. J. (1998). A spatiotemporal profile of visual system activation revealed by current source density analysis in the awake macaque. *Cereb Cortex* *8*, 575–592. doi:10.1093/cercor/8.7.575. 314
315
316
22. Van Kerkoerle, T., Self, M. W., and Roelfsema, P. R. (2017). Layer-specificity in the effects of attention and working memory on activity in primary visual cortex. *Nat Commun* *8*, 13804. doi:10.1038/ncomms13804. 317
318
319
23. Hubel, D. H., and Wiesel, T. N. (1962). Receptive fields, binocular interaction and functional architecture in the cat's visual cortex. *J Physiol* *160*, 106–154. doi:10.1113/jphysiol.1962.sp006837. 320
321
322
24. Reid, R., and Alonso, J.-M. (1995). Specificity of monosynaptic connections from thalamus to visual cortex. *Nature* *378*, 281–284. doi:10.1038/378281a0. 323
324
25. Angelucci, A., Bijanzadeh, M., Nurminen, L., Federer, F., Merlin, S., and Bressloff, P. C. (2017). Circuits and Mechanisms for Surround Modulation in Visual Cortex. *Annu Rev Neurosci* *40*, 425–451. doi:10.1146/annurev-neuro-072116-031418. 325
326
327
26. Dumoulin, S. O., and Knapen, T. (2018). How visual cortical organization is altered by ophthalmologic and neurologic disorders. *Annual Review of Vision Science* *4*, 357–379. doi:10.1146/annurev-vision-091517-033948. 328
329
330
27. Petridou, N., and Siero, J. C. (2019). Laminar fMRI: What can the time domain tell us? *NeuroImage* *197*, 761–771. doi:10.1016/j.neuroimage.2017.07.040. 331
332
28. Kok, P., Bains, L., van Mourik, T., Norris, D., and de Lange, F. (2016). Selective Activation of the Deep Layers of the Human Primary Visual Cortex by Top-Down Feedback. *Curr Biol* *26*, 371–376. doi:10.1016/j.cub.2015.12.038. 333
334
335
29. de Hollander, G., van der Zwaag, W., Qian, C., Zhang, P., and Knapen, T. (2021). Ultra-high field fMRI reveals origins of feedforward and feedback activity within laminae of human ocular dominance columns. *NeuroImage* *228*, 117683. doi:10.1016/j.neuroimage.2020.117683. 336
337
338
339

30. Huber, L., Finn, E. S., Chai, Y., Goebel, R., Stirnberg, R., Stöcker, T., Marrett, S., Uludag, K., Kim, S. G., Han, S. H., Bandettini, P. A., and Poser, B. A. (2021). Layer-dependent functional connectivity methods. *Prog Neurobiol* 207, 101835. doi:10.1016/j.pneurobio.2020.101835. 340 341 342 343
31. Raimondo, L., Oliveira, I. A., Heij, J., Priovoulos, N., Kundu, P., Leoni, R. F., and van der Zwaag, W. (2021). Advances in resting state fMRI acquisitions for functional connectomics. *NeuroImage* 243. doi:10.1016/j.neuroimage.2021.118503. 344 345 346
32. Oliveira, I. A. F., Cai, Y., Hofstetter, S., Siero, J. C. W., van der Zwaag, W., and Dumoulin, S. O. (2022). Comparing BOLD and VASO-CBV population receptive field estimates in human visual cortex. *NeuroImage* 248, 118868. doi:10.1016/j.neuroimage.2021.118868. 347 348 349
33. Oliveira, I. A. F., Siero, J. C. W., Dumoulin, S. O., and van der Zwaag, W. (2023). Improved Selectivity in 7 T Digit Mapping Using VASO-CBV. *Brain Topogr* 36, 23–31. doi:10.1007/s10548-022-00932-x. 350 351 352
34. Kashyap, S., Ivanov, D., Havlicek, M., Sengupta, S., Poser, B. A., and Uludağ, K. (2018). Resolving laminar activation in human V1 using ultra-high spatial resolution fMRI at 7T. *Sci Rep* 8, 17063. doi:10.1038/s41598-018-35333-3. 353 354 355
35. Polimeni, J. R., Renvall, V., Zaretskaya, N., and Fischl, B. (2018). Analysis strategies for high-resolution UHF-fMRI data. *NeuroImage* 168, 296–320. doi:10.1016/j.neuroimage.2017.04.053. 356 357 358
36. Yu, X., Qian, C., Chen, D. Y., Dodd, S. J., and Koretsky, A. P. (2014). Deciphering laminar-specific neural inputs with line-scanning fMRI. *Nat Methods* 11, 55–58. doi:10.1038/nmeth.2730. 359 360 361
37. Raimondo, L., Knapen, T., Oliveira, I. A., Yu, X., Dumoulin, S. O., van der Zwaag, W., and Siero, J. C. (2021). A line through the brain: implementation of human line-scanning at 7T for ultra-high spatiotemporal resolution fMRI. *J Cereb Blood Flow Metab* 41, 2831–2843. doi:10.1177/0271678X211037266. 362 363 364 365
38. Raimondo, L., Priovoulos, N., Passarinho, C., Heij, J., Knapen, T., Dumoulin, S. O., Siero, J. C., and van der Zwaag, W. (2023). Robust high spatio-temporal line-scanning fMRI in humans at 7T using multi-echo readouts, denoising and prospective motion correction. *J Neurosci Methods* 384, 109746. doi:10.1016/J.JNEUMETH.2022.109746. 366 367 368 369
39. Heij, J., Raimondo, L., Siero, J. C. W., Dumoulin, S. O., van der Zwaag, W., and Knapen, T. (2023). A selection and targeting framework of cortical locations for line-scanning fMRI. *Hum Brain Mapp* 44, 5471–5484. doi:10.1002/hbm.26459. 370 371 372
40. Jones, H. E., Grieve, K. L., Wang, W., and Sillito, A. M. (2001). Surround Suppression in Primate V1. *J Neurophysiol* 86, 2011–2028. doi:10.1152/jn.2001.86.4.2011. 373 374
41. Wang, T., Li, Y., Yang, G., Dai, W., Yang, Y., Han, C., Wang, X., Zhang, Y., and Xing, D. (2020). Laminar Subnetworks of Response Suppression in Macaque Primary Visual Cortex. *J Neurosci* 40, 7436–7450. doi:10.1523/JNEUROSCI.1129-20.2020. 375 376 377
42. Self, M. W., Lorteije, J. A., Vangeneugden, J., van Beest, E. H., Grigore, M. E., Levelt, C. N., Alexander Heimel, J., and Roelfsema, P. R. (2014). Orientation-Tuned Surround Suppression in Mouse Visual Cortex. *J Neurosci* 34, 9290–9304. doi:10.1523/JNEUROSCI.5051-13.2014. 378 379 380 381

43. Huber, L., Tse, D. H. Y., Wiggins, C. J., Uludağ, K., Kashyap, S., Jangraw, D. C., Bandettini, P. A., Poser, B. A., and Ivanov, D. (2018). Ultra-high resolution blood volume fMRI and BOLD fMRI in humans at 9.4 T: Capabilities and challenges. *NeuroImage* *178*, 769–779. doi:10.1016/j.neuroimage.2018.06.025. 382 383 384 385
44. Huber, L., Handwerker, D. A., Jangraw, D. C., Chen, G., Hall, A., Stüber, C., Gonzalez-Castillo, J., Ivanov, D., Marrett, S., Guidi, M., Goense, J., Poser, B. A., and Bandettini, P. A. (2017). High-Resolution CBV-fMRI Allows Mapping of Laminar Activity and Connectivity of Cortical Input and Output in Human M1. *Neuron* *96*, 1253–1263.e7. doi:10.1016/j.neuron.2017.11.005. 386 387 388 389 390
45. Huber, L., Finn, E. S., Handwerker, D. A., Bönstrup, M., Glen, D. R., Kashyap, S., Ivanov, D., Petridou, N., Marrett, S., Goense, J., Poser, B. A., and Bandettini, P. A. (2020). Sub-millimeter fMRI reveals multiple topographical digit representations that form action maps in human motor cortex. *NeuroImage* *208*, 116463. doi:10.1016/j.neuroimage.2019.116463. 391 392 393 394
46. Fracasso, A., Luijten, P. R., Dumoulin, S. O., and Petridou, N. (2018). Laminar imaging of positive and negative BOLD in human visual cortex at 7 T. *NeuroImage* *164*, 100–111. doi:10.1016/j.neuroimage.2017.02.038. 395 396 397
47. Koopmans, P. J., Barth, M., Orzada, S., and Norris, D. G. (2011). Multi-echo fMRI of the cortical laminae in humans at 7T. *NeuroImage* *56*, 1276–1285. doi:10.1016/j.neuroimage.2011.02.042. 398 399 400
48. Polimeni, J. R., Fischl, B., Greve, D. N., and Wald, L. L. (2010). Laminar analysis of 7T BOLD using an imposed spatial activation pattern in human V1. *NeuroImage* *52*, 1334–1346. doi:10.1016/j.neuroimage.2010.05.005. 401 402 403
49. Siero, J. C., Petridou, N., Hoogduin, H., Luijten, P. R., and Ramsey, N. F. (2011). Cortical depth-dependent temporal dynamics of the BOLD response in the human brain. *J Cereb Blood Flow Metab* *31*, 1999–2008. doi:10.1038/jcbfm.2011.57. 404 405 406
50. van der Zwaag, W., Francis, S., Head, K., Peters, A., Gowland, P., Morris, P., and Bowtell, R. (2009). fMRI at 1.5, 3 and 7 T: Characterising BOLD signal changes. *NeuroImage* *47*, 1425–1434. doi:10.1016/j.neuroimage.2009.05.015. 407 408 409
51. van Dijk, J. A., Fracasso, A., Petridou, N., and Dumoulin, S. O. (2020). Linear systems analysis for laminar fMRI: Evaluating BOLD amplitude scaling for luminance contrast manipulations. *Sci Rep* *10*, 5462. doi:10.1038/s41598-020-62165-x. 410 411 412
52. Rockland, K. S., and Pandya, D. N. (1979). Laminar origins and terminations of cortical connections of the occipital lobe in the rhesus monkey. *Brain Res* *179*, 3–20. doi:10.1016/0006-8993(79)90485-2. 413 414 415
53. Olsen, S. R., Bhandawat, V., and Wilson, R. I. (2010). Divisive Normalization in Olfactory Population Codes. *Neuron* *66*, 287–299. doi:10.1016/j.neuron.2010.04.009. 416 417
54. Reynolds, J. H., and Heeger, D. J. (2009). The Normalization Model of Attention. *Neuron* *61*, 168–185. doi:10.1016/j.neuron.2009.01.002. 418 419
55. Brouwer, G. J., Arnedo, V., Offen, S., Heeger, D. J., and Grant, A. C. (2015). Normalization in human somatosensory cortex. *J Neurophysiol* *114*, 2588–2599. doi:10.1152/jn.00939.2014. 420 421 422

56. Rabinowitz, N. C., Willmore, B. D. B., Schnupp, J. W. H., and King, A. J. (2011). Contrast Gain Control in Auditory Cortex. *Neuron* 70, 1178–1191. doi:10.1016/j.neuron.2011.04.030. 423 424 425
57. Callaway, E. M. (1998). Local circuits in primary visual cortex of the macaque monkey. *Annu Rev Neurosci* 21, 47–74. doi:10.1146/annurev.neuro.21.1.47. 426 427
58. Fitzpatrick, D., Lund, J. S., and Blasdel, G. G. (1985). Intrinsic connections of macaque striate cortex: afferent and efferent connections of lamina 4C. *J Neurosci* 5, 3329–3349. doi:10.1523/JNEUROSCI.05-12-03329.1985. 428 429 430
59. Xing, D., Yeh, C.-I., Burns, S., and Shapley, R. M. (2012). Laminar analysis of visually evoked activity in the primary visual cortex. *Proc Natl Acad Sci* 109, 13871–13876. doi:10.1073/pnas.1201478109. 431 432 433
60. Self, M. W., van Kerkoerle, T., Goebel, R., and Roelfsema, P. R. (2019). Benchmarking laminar fMRI: Neuronal spiking and synaptic activity during top-down and bottom-up processing in the different layers of cortex. *NeuroImage* 197, 806–817. doi:10.1016/j.neuroimage.2017.06.045. 434 435 436 437
61. Silva, A. C., Lee, S.-P., Iadecola, C., and Kim, S.-G. (2000). Early Temporal Characteristics of Cerebral Blood Flow and Deoxyhemoglobin Changes during Somatosensory Stimulation. *J Cereb Blood Flow Metab* 20, 201–206. doi:10.1097/00004647-200001000-00025. 438 439 440
62. Silva, A. C., and Koretsky, A. P. (2002). Laminar specificity of functional MRI onset times during somatosensory stimulation in rat. *Proc Natl Acad Sci* 99, 15182–15187. doi:10.1073/pnas.222561899. 441 442 443
63. Leprince, Y., Poupon, F., Delzescaux, T., Hasboun, D., Poupon, C., and Rivière, D. Combined Laplacian-equivolumic model for studying cortical lamination with ultra high field MRI (7 T). In: *2015 IEEE 12th International Symposium on Biomedical Imaging (ISBI) (2015):* (580–583). doi:10.1109/ISBI.2015.7163940. 444 445 446 447
64. Shamir, I., Tomer, O., Baratz, Z., Tsarfaty, G., Faraggi, M., Horowitz, A., and Assaf, Y. (2019). A framework for cortical laminar composition analysis using low-resolution T1 MRI images. *Brain Struct Funct* 224, 1457–1467. doi:10.1007/s00429-019-01848-2. 448 449 450
65. Trampel, R., Bazin, P.-L., Pine, K., and Weiskopf, N. (2019). In-vivo magnetic resonance imaging (MRI) of laminae in the human cortex. *NeuroImage* 197, 707–715. doi:10.1016/j.neuroimage.2017.09.037. 451 452 453
66. Godenschweger, F., Kägebein, U., Stucht, D., Yarach, U., Sciarra, A., Yakupov, R., Lüsebrink, F., Schulze, P., and Speck, O. (2016). Motion correction in MRI of the brain. *Phys Med Biol* 61, R32–R56. doi:10.1088/0031-9155/61/5/R32. 454 455 456
67. Zaitsev, M., Maclaren, J., and Herbst, M. (2015). Motion artifacts in MRI: A complex problem with many partial solutions. *J Magn Reson* 42, 887–901. doi:10.1002/jmri.24850. 457 458
68. Priovoulos, N., Roos, T., Ipek, O., Meliado, E. F., Nkrumah, R. O., Klomp, D. W., and van der Zwaag, W. (2021). A local multi-transmit coil combined with a high-density receive array for cerebellar fMRI at 7T. *NMR Biomed* 34, e4586. doi:10.1002/nbm.4586. 459 460 461
69. Petridou, N., Italiaander, M., van de Bank, B. L., Siero, J. C., Luijten, P. R., and Klomp, D. W. (2013). Pushing the limits of high-resolution functional MRI using a simple high-density multi-element coil design. *NMR Biomed* 26, 65–73. doi:10.1002/nbm.2820. 462 463 464

70. Alvarez, I., De Haas, B., Clark, C., Rees, G., and Schwarzkopf, D. (2015). Comparing different stimulus configurations for population receptive field mapping in human fMRI. *Front Hum Neurosci* 9. 465
71. Lage-Castellanos, A., Valente, G., Senden, M., and De Martino, F. (2020). Investigating the Reliability of Population Receptive Field Size Estimates Using fMRI. *Front Neurosci* 14. 468
72. Senden, M., Reithler, J., Gijsen, S., and Goebel, R. (2014). Evaluating Population Receptive Field Estimation Frameworks in Terms of Robustness and Reproducibility. *PLoS ONE* 9, e114054. doi:10.1371/journal.pone.0114054. 470
73. van Dijk, J. A., de Haas, B., Moutsiana, C., and Schwarzkopf, D. S. (2016). Intersession reliability of population receptive field estimates. *NeuroImage* 143, 293–303. doi:10.1016/j.neuroimage.2016.09.013. 473
74. Bianciardi, M., Fukunaga, M., van Gelderen, P., Horovitz, S. G., de Zwart, J. A., Shmueli, K., and Duyn, J. H. (2009). Sources of functional magnetic resonance imaging signal fluctuations in the human brain at rest: a 7 T study. *Magn Reson Imaging* 27, 1019–1029. doi:10.1016/j.mri.2009.02.004. 476
75. Raimondo, L., Heij, J., Knapen, T., Dumoulin, S. O., van der Zwaag, W., and Siero, J. C. W. (2023). Towards functional spin-echo BOLD line-scanning in humans at 7T. *Magn Reson Mater Phy*. doi:10.1007/s10334-022-01059-7. 480
76. Triantafyllou, C., Hoge, R., Krueger, G., Wiggins, C., Potthast, A., Wiggins, G., and Wald, L. (2005). Comparison of physiological noise at 1.5 T, 3 T and 7 T and optimization of fMRI acquisition parameters. *NeuroImage* 26, 243–250. doi:10.1016/j.neuroimage.2005.01.007. 483
77. Benson, N. C., Jamison, K. W., Arcaro, M. J., Vu, A. T., Glasser, M. F., Coalson, T. S., Van Essen, D. C., Yacoub, E., Ugurbil, K., Winawer, J., and Kay, K. (2018). The Human Connectome Project 7 Tesla retinotopy dataset: Description and population receptive field analysis. *J Vis* 18, 23. doi:10.1167/18.13.23. 487
78. Gorgolewski, K. J., Auer, T., Calhoun, V. D., Craddock, R. C., Das, S., Duff, E. P., Flandin, G., Ghosh, S. S., Glatard, T., Halchenko, Y. O., Handwerker, D. A., Hanke, M., Keator, D., Li, X., Michael, Z., Maumet, C., Nichols, B. N., Nichols, T. E., Pellman, J., Poline, J.-B., Rokem, A., Schaefer, G., Sochat, V., Triplett, W., Turner, J. A., Varoquaux, G., and Poldrack, R. A. (2016). The brain imaging data structure, a format for organizing and describing outputs of neuroimaging experiments. *Sci Data* 3, 160044. doi:10.1038/sdata.2016.44. 491
79. Peirce, J. W. (2007). PsychoPy—Psychophysics software in Python. *J Neurosci Methods* 162, 8–13. doi:10.1016/J.JNEUMETH.2006.11.017. 497
80. Dale, A. M. (1999). Optimal experimental design for event-related fMRI. *Hum Brain Mapp* 8, 109–114. doi:10.1002/(SICI)1097-0193(1999)8:2/3<109::AID-HBM7>3.0.CO;2-W. 499
81. Mumford, J. A., Poline, J.-B., and Poldrack, R. A. (2015). Orthogonalization of Regressors in fMRI Models. *PLoS ONE* 10, e0126255. doi:10.1371/journal.pone.0126255. 501
82. Chen, G., Taylor, P. A., Reynolds, R. C., Leibenluft, E., Pine, D. S., Brotman, M. A., Pagliaccio, D., and Haller, S. P. (2023). BOLD Response is more than just magnitude: Improving detection sensitivity through capturing hemodynamic profiles. *NeuroImage* 277, 120224. doi:10.1016/j.neuroimage.2023.120224. 503

83. Gao, J. S., Huth, A. G., Lescroart, M. D., and Gallant, J. L. (2015). Pycortex: an interactive surface visualizer for fMRI. *Front Neuroinform* 9. 507
508
84. Savitzky, A., and Golay, M. J. E. (1964). Smoothing and Differentiation of Data by Simplified Least Squares Procedures. *Anal. Chem.* 36, 1627–1639. doi:10.1021/ac60214a047. 509
510
85. Vallat, R. (2018). Pingouin: statistics in Python. *JOSS* 3, 1026. doi:10.21105/joss.01026. 511
86. Seabold, S., and Perktold, J. statsmodels: Econometric and statistical modeling with python. In: *9th Python in Science Conference* (2010):. 512
513

| | |
|--|--|
| STAR METHODS | 514 |
| Key resources table | 515 |
| A KRT has been included as a file called KRT.docx | 516 |
| Resource availability | 517 |
| Lead contact | 518 |
| Requests for further information and resources should be directed to and will be fulfilled by the lead contact, Jurjen Heij (j.heij@herseninstituut.knaw.nl). | 519 520 |
| Materials availability | 521 |
| This study did not generate new unique reagents. | 522 |
| Data and code availability | 523 |
| <ul style="list-style-type: none"> • Data in BIDS-format⁷⁸ will be made available on request in compliance with GDPR regulations. • The code for this paper is available in the following repositories: Preprocessing of fMRI, anatomical pipeline, and handling of line-scanning data: https://github.com/gjheij/linescanning. Line-scanning experiment: https://github.com/gjheij/LineExps/tree/main/ActNorm3. Analysis: https://github.com/spinoza-centre/holeresponse. • Any additional information required to reanalyze the data reported in this paper is available from the lead contact upon request. | 524 525 526 527 528 529 530 531 |
| Experimental model and study participant details | 532 |
| 13 participants (ages 23–50 years, 5 female) participated in this study. All participants had normal or corrected-to normal visual acuity, were screened prior to the experiments to ensure MR compatibility, and provided written informed consent as approved by the ethics committee of the Vrije Universiteit Amsterdam. Some participants were scanned twice targeting a different pRF, resulting in a total of 18 individually sampled cortical patches. | 533 534 535 536 537 |
| Method details | 538 |
| Experimental setup | 539 |
| The visual stimuli were generated using the Psychopy package ⁷⁹ wrapped in exptools2 (https://github.com/gjheij/exptools2). Stimuli were displayed on an MRI-compatible screen located outside the bore (Cambridge Research Systems 32" LCD widescreen, 1920×1080 resolution, 120Hz refresh rate), viewed by the participants through front-silvered mirrors (example stimuli shown in Figure 2A). Each stimulus presentation consisted of a 8Hz flickering stimulus for 2 seconds. The inter-stimulus intervals (ISIs) were jittered following a negative exponential decay to reduce collinearity between subsequent events ^{80–82} and spaced far apart to allow epoching strategies. $ISI_{min}/ISI_{max}/ISI_{mean} = 14s/24s/18s$, resulting in 5 stimulus presentations per stimulus | 540 541 542 543 544 545 546 547 |

per run (7 minutes). To maximize SNR while limiting predictability, we simulated two sets of stimulus presentation orders and stimulus intervals. These two flavors were randomly presented to the participants during the session. Participants' engagement was ensured by presenting a small fixation dot in the middle of the stimulus that changed color (red-green) following a negative exponential decay ($ISI_{\min}/ISI_{\max}/ISI_{\text{mean}} = 4\text{s}/8\text{s}/6\text{s}$) and was monitored via an EyeLink 1000 eye-tracker system at 1000Hz (<https://www.sr-research.com/>). Participants were instructed to report this change of color via a button press.

Vertex selection

Similar to our previous approach³⁹, vertex selection was implemented using surface processing procedures from pycortex⁸³. We aimed to find a vertex with primary visual cortex (manually delineated based on polar angle maps) in the eccentricity band subtending 1.5-3 dva, at least 1 dva away from the vertical meridian, sufficient variance explained (>0.55), and reasonable pRF sizes ($>0.50\text{dva}$). A binary mask representing surviving vertices was visually inspected using FreeSurfer's FreeView. From this mask, we selected a vertex within a blob that was located favorably with respect to curvature as well as surrounding vertices. This ensured that responses from similarly behaving pRFs would be projected into the line.

Data acquisition

The workflow includes two separate scan sessions typically acquired on different days. The first session is dedicated to the acquisition of anatomical information and whole-brain population receptive field (pRF) estimation (see ref³⁹ for acquisition and experimental paradigm). In the second session, we perform our functional line-scanning experiment, targeting a specific location on the cortical surface.

The line-scanning functional acquisition used a modified multi-echo 2D gradient-echo sequence where the phase-encoding gradients are removed and two OVS bands are used to suppress signals outside the line^{37,38}. With this sequence, $94.3 \pm 1.3\%$ of undesired signal outside the region of interest is suppressed^{37,38}. A gap of 4 mm between the two OVS bands was used, resulting in a nominal resolution for the line of $4 \times 2.5 \times 0.25 \text{ mm}^3$; thus, 0.25 mm in the laminar direction. Other parameters were: $TR/TE_{1-5} = 105 \text{ ms}/6 \text{ ms}, 14 \text{ ms}, 22 \text{ ms}, 30 \text{ ms}, 38 \text{ ms}$, readout bandwidth = 131.4 Hz/pixel, $FA = 16^\circ$ ³⁸. Data were acquired using two custom-built high-density 16-channel surface coils arrays (total 32 channels) for signal reception^{68,69} and the NOVA coil for transmission (Nova Medical, Wilmington, MA). The gradient coil has a maximum amplitude of 40 mT/m and a 200 T/m/s maximum slew rate.

For registration, a 4-min whole-brain T_1 -weighted scan was acquired using the two-channel transmit coil to receive (Nova Medical, Wilmington, MA), at a resolution of 1.5 mm isotropic ($FOV = 245 \times 245 \times 184 \text{ mm}^3$, matrix = $164 \times 163 \times 184$, $TR/TE = 6.2 \text{ ms}/3 \text{ ms}$, $FA_1/FA_2 = 5^\circ/7^\circ$, $TR_{MP2RAGE}/TI_1/TI_2 = 5500 \text{ ms}/800 \text{ ms}/2700 \text{ ms}$). Two short additional scans accompanied the line-scanning acquisition: for the nominal line representation, a slice image with phase-encoding, but without OVS bands, was acquired. For line coil sensitivity maps used when reconstructing line-scanning data, a slice image with phase encoding and with OVS bands was acquired.

Data reconstruction and quality assessment

The reconstruction of the line-scanning data was performed offline using MATLAB Gyrotools. We combined the multichannel coil data with a temporal signal-to-noise ratio (tSNR) and coil sensitivity-weighted SoS weighted scheme per echo^{37,38}. Multi-echo data were then combined

with a sum of squares operation³⁸. We presented the stimuli using two different orders to avoid habituation. To deal with high frequency noise, we low-passed the data with a Savitzky-Golay filter⁸⁴ (31 samples and 3rd order) before averaging runs with the same stimulus ordering. Line-scanning fMRI is particularly prone to movement due to the extreme loss of coverage. Our participant pool consisted of highly experienced participants. Movement was further restricted by taping the chin to the transmit coil. Then, we defined the target area of interest by manually delineating the CSF/gray matter boundary and gray/white matter boundary on a run-to-run basis using the anatomical reference slice. For each event, we then extracted and averaged the time period 2 seconds prior to onset until 14 seconds after (Figure S7AC). This resulted in an average response to each stimulus for each participant across the different stimulus orders (Figure 79B). Indeed, based on the responses across the entire line, we concluded that the stimuli evoked the most specific responses in the target area (Figure S7D).

The cortical locations were included if two criteria were met (Figure S8). First, the response to the center stimulus had to be larger than the other stimuli. Second, this stimulus had to show the draining vein effect across depth. We defined the target area of interest by manually delineating the CSF/gray matter boundary and gray/white matter boundary on a run-to-run basis using the anatomical reference slice. To verify these voxels were properly responsive, we used a GLM with canonical HRF, where the prediction based on the center stimulus events was entered as regressor. This resulted in a variance explained across the line, allowing us to verify where the largest responses were indeed near the intended target location. For depth profiles, we estimated the magnitude evolution within a 5-7 second window after stimulus onset. Given that the cortical depth was covered by a varying number of data points across participants, we regridded the data so that cortical depth was covered by 20 data points^{30,43–45}. In cases of slight discrepancies between the chosen data points and the variance explained, an additional shift was applied to the voxel selection. In some participants, the adjustment procedure resulted in cleaner responses to the center stimulus and improved draining vein profile (black profiles). From the 18 individually sampled pRF responses, 11 (defined as n) were eventually entered into the final analysis. Note that this procedure only further improved the precision of the presented results by boosting statistical power (increased n); the results remained the same without this procedure (Figure S3B).

Quantification and statistical analysis

Significance testing was performed using the python packages Pingouin⁸⁵ and statsmodels⁸⁶. For each comparison, we performed tests for normality and homogeneity of variance. Based on the outcome, the appropriate test was selected (parametric or non-parametric). For within-participant comparisons of stimulus responses, individual paired-samples t-tests were used. Group comparisons were performed using ANOVA with Holm-corrected post-hoc test (if applicable). The significance level was set to $\alpha=0.05$. Unless specified otherwise, standard error of the mean (SEM) was used to quantify precision. The specific tests, significance levels, and precision measurements are reported in-text and/or in the figure captions.